

Supporting Information

Morphology Independent Stable White-Light Emission from Self-Assembled 2D Perovskites Driven by Strong Exciton-Phonon Coupling to the Organic Framework

Krishnamoorthy Thirumal, Wee Kiang Chong, Wei Xie, Rakesh Ganguly, Subas Kumar Muduli, Matthew Sherburne, Mark Asta, Subodh Mhaisalkar, Tze Chien Sum, Han Sen Soo, Nripan Mathews*.*

Precursor Materials. Lead (II) chloride, phenethylamine, octylamine, and hydrochloric acid (37%) were purchased from Sigma-Aldrich. All solvents used in this study were also purchased from Sigma-Aldrich. All reagents and solvents were used without further purification unless otherwise stated. Spectroscopic grade solvents were used in the UV-Vis and photoluminescence spectroscopic measurements.

Single Crystal Growth. Phenethylammonium chloride was prepared by slowly mixing a stoichiometric amount of hydrochloric acid with phenethylamine dissolved in methanol at 0 °C. After stirring the solution for an hour, the solvents were removed using a rotary evaporator at low pressure and at 60 °C. If necessary, excess methanol was added to form an azeotropic mixture with water to remove the latter completely. The solid thus produced was washed with diethyl ether to remove the unreacted amine. Finally, the ammonium salt was dried under vacuum at 50 °C overnight. Single crystals of $(\text{C}_6\text{H}_5\text{C}_2\text{H}_4\text{NH}_3)_2\text{PbCl}_4$ were grown by vapor diffusion of nitromethane into a solution formed of 2 equivalents of $\text{C}_6\text{H}_5\text{C}_2\text{H}_5\text{NH}_3\text{Cl}$ and 1 equivalent of PbCl_2 in N,N-dimethylformamide (DMF) around 25 °C. After a week, a few

platelets of $(\text{C}_6\text{H}_5\text{C}_2\text{H}_4\text{NH}_3)_2\text{PbCl}_4$ were formed with good quality. The solubility of PEPC is good in DMSO, but it has the ability to form coordination bonds with lead (Pb). Hence, it is not desirable to grow a single crystal from DMSO solutions. Many other anti-solvents like diethylether, 1,2-dimethoxyethane, and ethanol were also used but they all led to the formation of poor quality crystals. These crystals were used for single-crystal X-ray diffraction (XRD) measurements and also for ultrafast optical spectroscopy studies. [CCDC 1498513 contains the supplementary crystallographic data for this paper. These data can be obtained free of charge from The Cambridge Crystallographic Data Centre via www.ccdc.cam.ac.uk/data_request/cif

Solution and Sample Preparation. A solution of phenethylammonium lead chloride ($(\text{C}_6\text{H}_5\text{C}_2\text{H}_4\text{NH}_3)_2\text{PbCl}_4$) was prepared by dissolving 2 mmol of phenethylammonium chloride and 1 mmol of lead chloride in DMSO. Final concentrations of the solutions were fixed at 1.0 and 0.20 molar levels. These two solutions were spin-coated on ITO substrates at 4000 rpm for 30 seconds, followed by annealing at 100 °C for 30 mins. These as-prepared thin films were used for XRD, FESEM, UV-Vis, and photoluminescence studies. The powder sample of $\text{PEA}_2\text{PbCl}_4$ was prepared by drop-casting a sol-gel solution of $(\text{C}_6\text{H}_5\text{C}_2\text{H}_4\text{NH}_3)_2\text{PbCl}_4$ on a glass substrate and dried at 100 °C for a few hours. The powdery material was finely grinded and used for XRD measurements.

Nanoparticle Synthesis. PbCl_2 (0.100 mmol, 27.8 mg) along with phenethylamine (0.24 mmol, 29.0 mg) and octylamine (0.16 mmol, 26.4 μl) were dissolved in 500 μl of DMF followed by the addition of hydrochloric acid (50 μl). The reaction mixture was sonicated for a few minutes to form a clear solution. Around 200 μl of this solution was later slowly added into a 2 ml hexane solvent under vigorous stirring at room temperature. This mixture was further stirred for five minutes. Quick addition of acetone to this mixture led to nanoparticles of $(\text{C}_6\text{H}_5\text{C}_2\text{H}_4\text{NH}_3)_2\text{PbCl}_4$.

Powder X-ray diffraction. The phase purity was confirmed by powder X-ray diffraction (PXRD) measurements collected with a Bruker D8 Advance diffractometer (Bragg-Brentano geometry) equipped with a Cu K α X-ray tube operated at 40 kV and 40 mA, scanned using a step size of 0.02° and a time per step of 1 s.

X-ray Single Crystallographic Analyses. The crystals of PEPC were found to be twinned; the twin law and cell parameters were determined using the program CELL_NOW,¹ and the reflection data were processed and corrections applied using the program TWINABS.² The twin law is given by -1 0 0 0 1 0 0 -0.5 -1. Some of the Pb and Cl ions were found to be disordered and were refined over two positions with occupancy of ~0.83 and ~0.17. One of the amino group was also disordered over two positions with the occupancy of ~0.56 and ~0.44. The ethyl groups were, as expected, disordered and appropriate restraints and constraints (SIMU, ISOR and RIGU) were used. One of the reflections (0 0 1) that was affected by beam stop was omitted.

Density Functional Theory Calculations. First-principles calculations were performed on two 188-atom primitive unit cells according to the space group and atomic coordinates of PEPC determined above, as visualized in Figure S2. The two structures represent the two preferred orientations of the phenethylammonium (PEA) organic cations with respect to the inorganic layers of the PbCl₆ octahedra. In Figure S2, the orientations are differentiated, keeping C, N, and H atoms fixed, while changing Pb and Cl by placing them only on select atomic sites that were experimentally indexed to have partial occupancies.

All calculations were performed within the framework of Density Functional Theory (DFT)²⁻⁴ using version 5.4.1 of the Vienna *Ab initio* Simulation Package (VASP).⁵⁻⁶ The calculations made use of the Generalized Gradient Approximation (GGA) for the exchange-correlation functional, due to Perdew, Burke and Ernzerhof (PBE)⁷. The electron-ion interactions were described with

the projector-augmented-wave (PAW) method⁸ as implemented in VASP by Kresse and Joubert.⁹ PAW potentials labeled “C 08Apr2002”, “N 08Apr2002”, “H 15Jun2001”, “Pb_d 06Sep2000”, and “Cl 06Sep2000”, treating $2s^22p^2$, $2s^22p^3$, $1s^1$, $6s^25d^{10}6p^2$ and $3s^23p^5$ as valence electrons, were employed for C, N, H, Pb and Cl, respectively. A plane wave cutoff energy of 500 eV was used for the expansion of wavefunctions, and the Brillouin zone was sampled using Γ -centered k -point meshes of $3\times3\times2$ and $4\times4\times3$, as generated using the Monkhorst–Pack scheme¹⁰, for structural relaxations and single point calculations, respectively. Tests using higher plane wave cutoff energies and denser k -point meshes showed such settings lead to total energies that converged to within 1 meV/cell. Partial occupancies were set using Gaussian smearing with a smearing width of 0.05 eV for structural relaxations, and the tetrahedron method with Blöchl corrections¹¹ for single point calculations. The electronic and ionic optimizations were performed using the Davidson-block algorithm¹² and the Conjugate-gradient algorithm,¹³ using 1×10^{-5} eV/cell energy and 0.02 eV/Å force thresholds as the convergence criteria, respectively. The projection operators were evaluated in real space. Spin-polarization was allowed in all calculations but no local moments were observed. Scalar-relativistic mass-velocity and Darwin corrections were included in all calculations following previous references.¹⁴⁻¹⁵. In more accurate calculations, the spin-orbit coupling (SOC) effect was included, and corrections for van der Waals (vdW) interactions were incorporated using the method of Tkatchenko and Scheffler¹⁶ with iterative Hirshfeld partitioning.¹⁷ The electronic band structure was evaluated along the special k -point paths in the Brillouin zone of a TRI_{1b} lattice following Setyawan and Curtarolo.¹⁸ Note that Γ -M is the direction perpendicular to the inorganic layer (M is labeled Z e.g. in Bilbao Crystallographic Server¹⁹). Crystal structures were visualized with VESTA²⁰.

UV-Vis Spectroscopy and Scanning Electron Microscopy. UV-Vis absorption spectra were collected with a Shimadzu UV3600 spectrophotometer. Surface morphology images were recorded using field emission scanning electron microscope (FESEM, JEOL, JSM-7600F, 5 kV).

Photoelectron Spectroscopy in Air. Photoelectron spectroscopy in air (PESA) measurements were conducted with a Riken Keiki AC-2 spectrometer with a power setting of 800 nW and a power number of 0.5. A thin film of perovskite on ITO was used for the PESA analysis. Thermogravimetric analysis was performed on a TGA Q500 V6.7 (TA Instruments) over a temperature range from 22 °C to 800° C at a ramp of 10 °C/min under nitrogen flux of 60 mL/min. Differential scanning calorimetry (DSC) was conducted on a Q10 V9.9 build calorimeter (TA Instruments) at a rate of 10 °C/min under nitrogen flow rate of 60 ml/min. The minimum temperature was -80 °C and the maximum temperature was 180 °C, which is well below the degradation temperature of the compound. AFM measurements were conducted using a Bruker Icon microscope. All measurements were performed in the standard tapping mode with OTESPA-R3 tips from Bruker.

Steady-State and Time-Resolved Photoluminescence (PL) Spectroscopy. The laser wavelength (340 nm) used for PL measurement is generated using a Coherent OPerA-Solo optical parametric amplifier from a 800 nm input pulse laser. The 800 nm pulse laser originates from a Coherent Libra regenerative amplifier (1 KHz, 50 fs, 800 nm) seeded by a Coherent Vitesse oscillator (50 fs, 80 MHz). For all measurements, the 340 nm excitation beam is passed through a short pass filter to remove residual 800 nm photons in the beam. For steady-PL measurements, the emission is collected using a backscattered PL configuration and dispersed using a 300 g/mm spectrometer (Acton, Spectra Pro 2500i). To prevent a second order diffracted

laser peak (due to the grating) from appearing in the PL spectrum at 680 nm, a long pass filter is also used to remove any scattered laser radiation in the emission. In addition, spectral corrections using monochromator and charge-coupled device (CCD) response functions were also carried out to obtain the final PL spectra. PL quantum efficiency (PLQE) measurements were conducted using an integrating sphere and the PLQE values were calculated after taking into account monochromator and charge-coupled device (CCD) response functions. For time-resolved PL measurements, the back-scattered emissions were temporally resolved using an Optronis OptoscopeTM streak camera system with an ultimate ~ 10 ps resolution at the fastest scan speed.

Transient Absorption (TA) Measurements. The laser wavelength (340 nm) used for TA measurement is generated using a Light Conversion TOPAS-C optical parametric amplifier from a 800 nm input pulse laser. The 800 nm pulse laser originates from a Coherent Legend regenerative amplifier (1 KHz, 150 fs, 800 nm) seeded by a Coherent Vitesse oscillator (100 fs, 80 MHz). Visible probe ($\sim 420 - 750$ nm) femtosecond TA spectra were taken with the Ultrafast System HELIOS TA spectrometer. The visible probe pulses were generated by focusing a small portion of the fundamental 800 nm laser pulses into a sapphire plate. Any unconverted residual 800 nm pump and probe pulses were removed using an optical filter before directing at the sample.

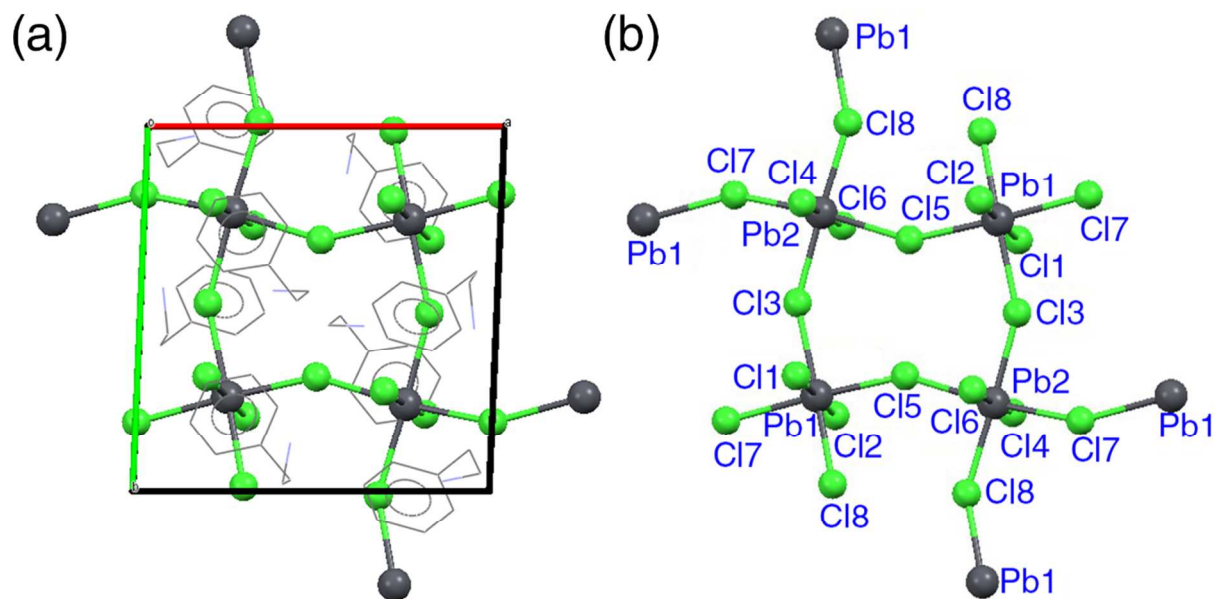


Figure S1. Crystal structure showing the arrangement of the organic ammonium cations intercalated between the 2D inorganic layers in PEPC viewed along the c-axis (a) with and (b) without the phenethylammonium cation shown. The Pb atoms are in grey, while the chloride atoms are in green.

Table S1. X-ray crystallographic and refinement data for PEPC

Identification code	shs183x	
Empirical formula	C ₃₂ H ₄₈ Cl ₁₈ N ₄ Pb ₂	
Formula weight	1186.72	
Temperature	273(2) K	
Wavelength	0.71073 Å	
Crystal system	Triclinic	
Space group	P-1	
Unit cell dimensions	a = 11.1152(3) Å	a = 99.1730(10)°.
	b = 11.2048(3) Å	b = 104.5250(10)°.
	c = 17.5909(5) Å	g = 90.0030(10)°.
Volume	2091.85(10) Å ³	
Z	2	
Density (calculated)	1.884 Mg/m ³	
Absorption coefficient	8.576 mm ⁻¹	
F(000)	1136	
Crystal size	0.240 x 0.180 x 0.120 mm ³	
Theta range for data collection	1.843 to 27.176°.	
Index ranges	-14 ≤ h ≤ 13, -14 ≤ k ≤ 14, 0 ≤ l ≤ 22	
Reflections collected	17496	
Independent reflections	9197 [R(int) = 0.1067]	
Completeness to theta = 25.242°	99.0 %	
Refinement method	Full-matrix least-squares on F ²	
Data / restraints / parameters	9197 / 472 / 462	
Goodness-of-fit on F ²	1.081	
Final R indices [I > 2σ(I)]	R1 = 0.0625, wR2 = 0.1628	
R indices (all data)	R1 = 0.0684, wR2 = 0.1705	
Extinction coefficient	n/a	
Largest diff. peak and hole	2.819 and -2.018 e.Å ⁻³	

Table S2. Band gap, total energy, atomic volume, and lattice parameters of PEPC.

	Orientation	vdW	SOC	Band gap ² (eV)	Total energy ³ (eV/cell)	Atomic volume (Å ³ /cell)	a (Å)	b (Å)	c (Å)	α (°)	β (°)	γ (°)
Theory ¹ (DFT-GGA)	1	no	no	3.18	12.614	2237.3	11.26	11.37	18.23	99.0	103.8	90.0
	1	no	yes	2.39	11.213	2236.2	11.25	11.37	18.23	99.0	103.8	90.0
	1	yes	no	3.07	1.419	2047.0	11.00	11.11	17.46	99.2	103.5	90.0
	1	yes	yes	2.27	0.000	2046.8	11.00	11.11	17.47	99.2	103.5	90.0
	2	no	no	3.12	13.006	2303.7	11.31	11.39	18.68	98.7	104.1	90.0
	2	no	yes	2.39	11.509	2323.2	11.28	11.37	18.84	98.7	103.2	90.0
	2	yes	no	3.01	2.070	2111.2	11.14	11.17	17.62	99.1	102.6	90.0
	2	yes	yes	2.11	0.638	2111.2	11.14	11.17	17.62	99.1	102.6	90.0
Experiment				3.56 ^b		2091.9	11.12	11.20	17.59	99.2	104.5	90.0

¹Values calculated with vdW and SOC are given in shaded cells and bold fonts, respectively.

²Optical and fundamental (electronic) band gap from theory and experiment, respectively.

³All referenced to the value for orientation 1 calculated with vdW and SOC.

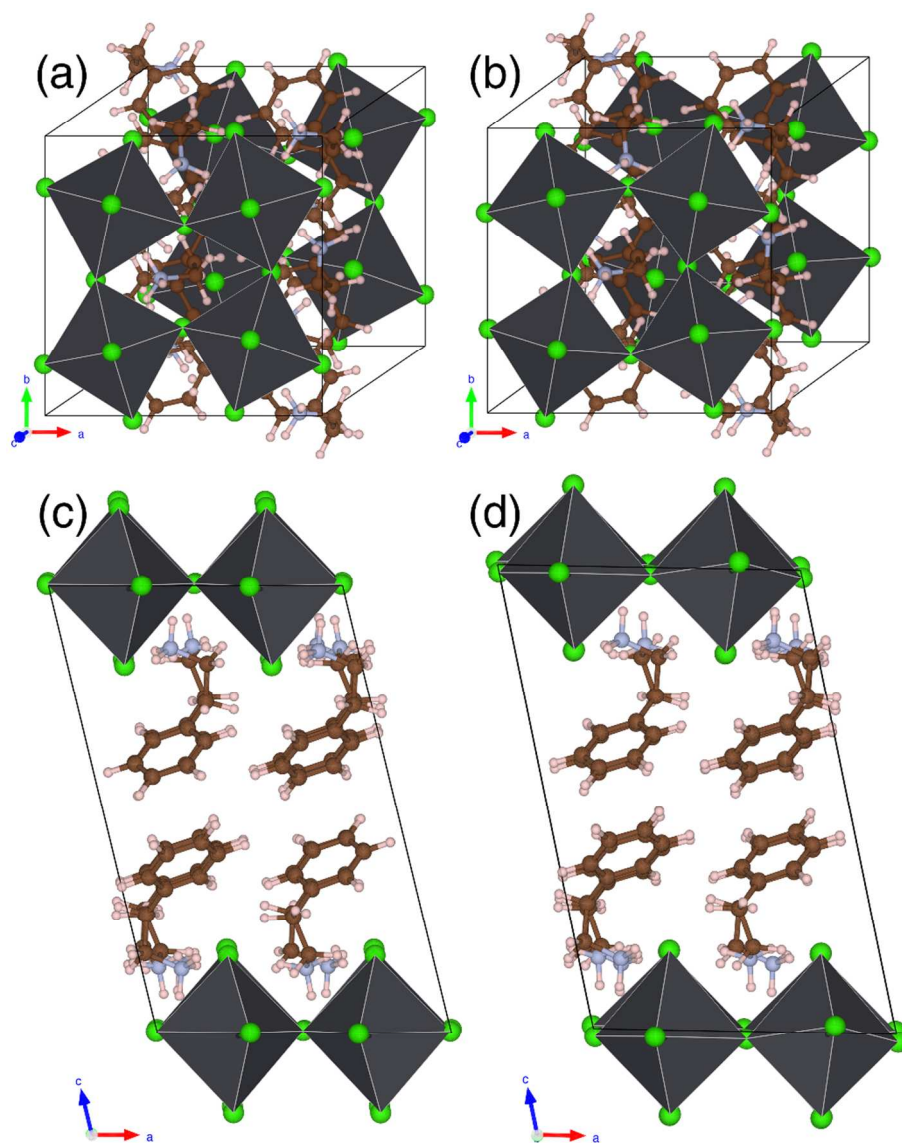


Figure S2 Crystal structures of PEPC after full relaxation in DFT-GGA calculations (with vdW and SOC), viewed along $a \times b$ in panels (a) and (b), and along b directions in panels (c) and (d). Orientation 1 is in panels (a) and (c), while 2 is in panels (b) and (d).

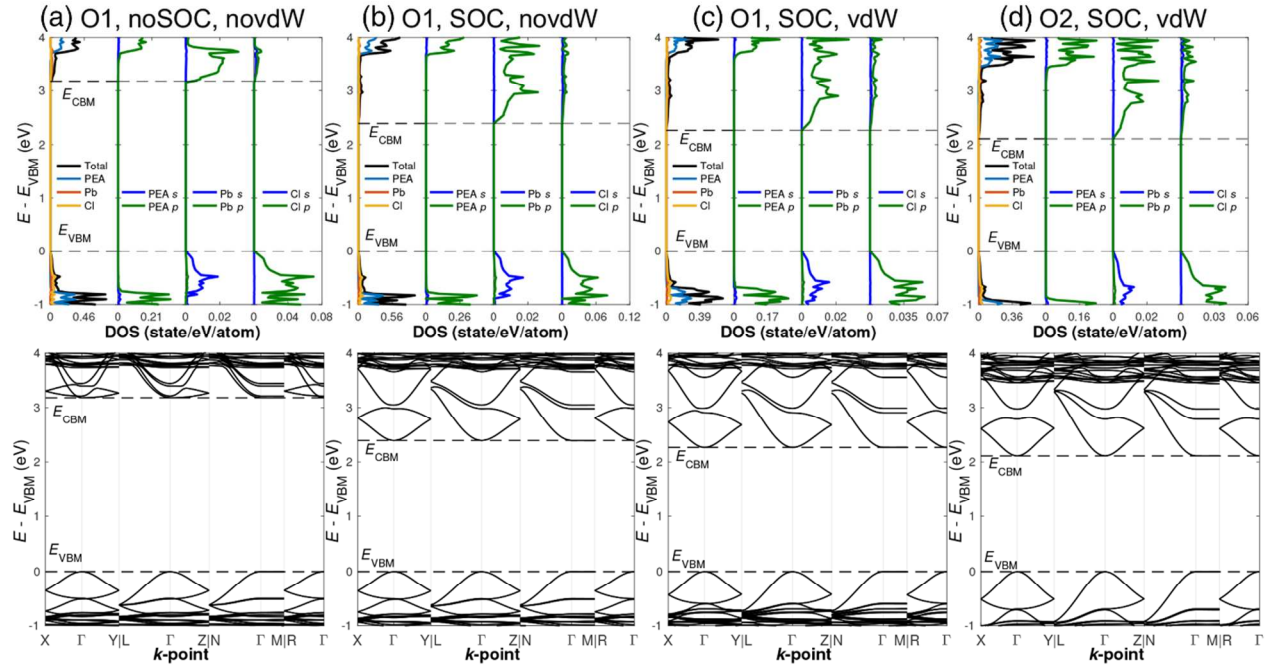


Figure S3. Electronic density of states (top row) and band structure (bottom row) of PEPC in orientation 1 (panels (a)-(c)) and 2 (panel (d)). In the panel labels, O1 and O2 denote orientations 1 and 2, no SOC and SOC denote without and with Spin orbit coupling included, while no vdW and vdW denote without and with van der Waals correction added, respectively. Note that in each panel the axis scale for the total/site projected DOS (the left most sub-axis) is different from those for the orbital projected DOS (the three sub-axes to the right)

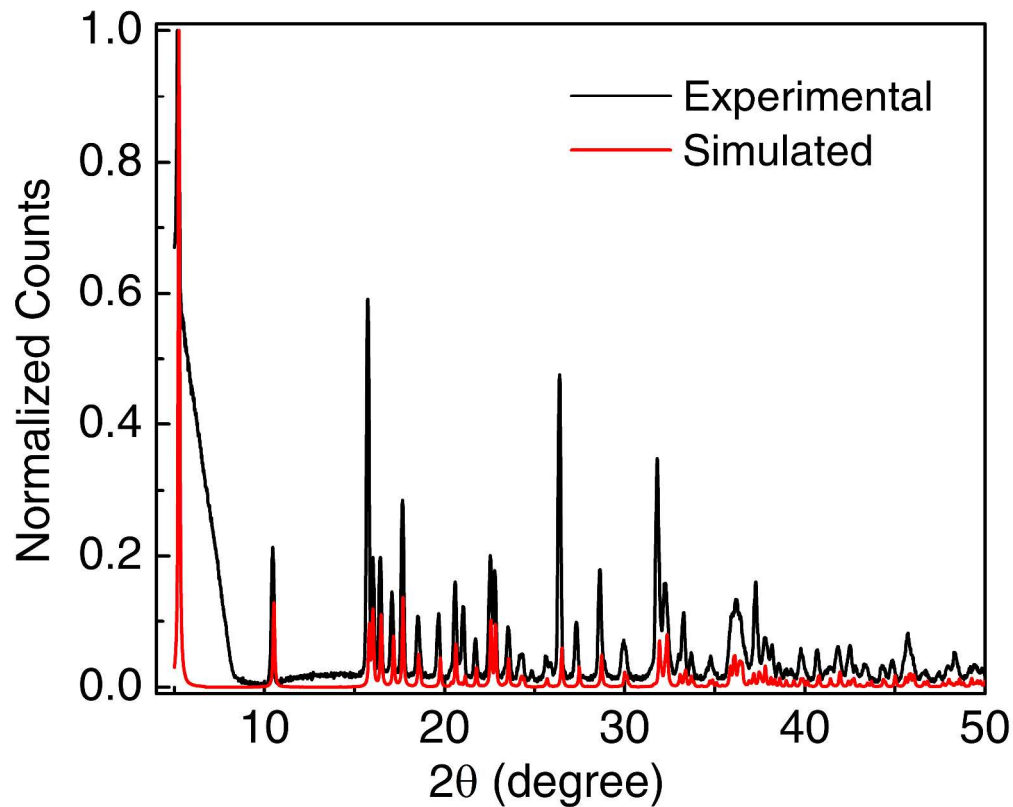


Figure S4. Powder XRD pattern of a finely ground powder sample of PEPC and the simulated XRD pattern from the single crystal data.

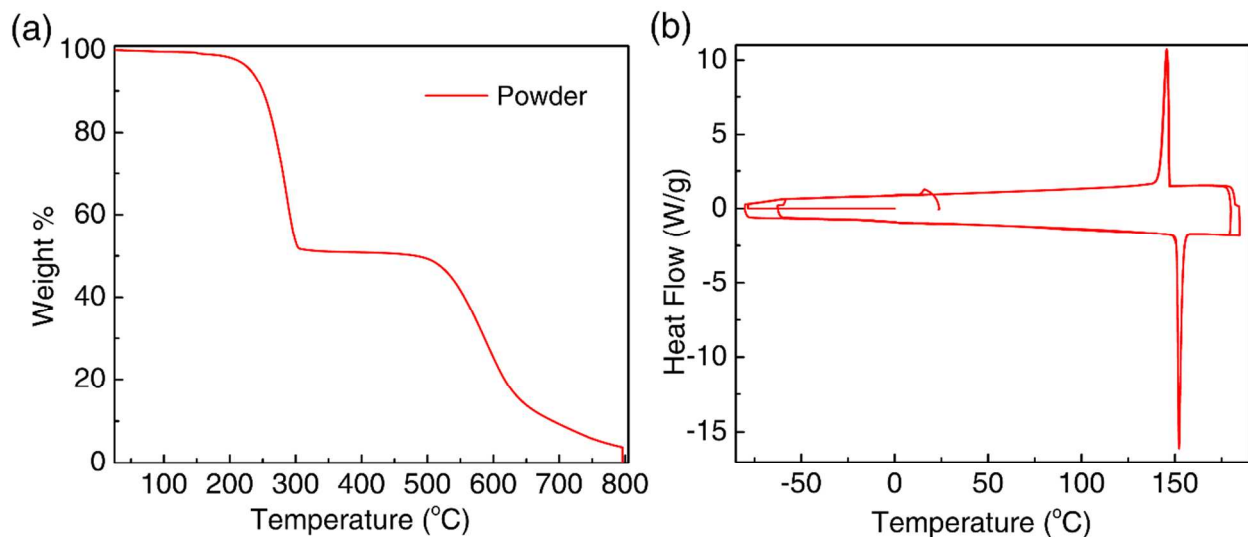


Figure S5. (a) Thermogravimetric analysis and (b) Differential scanning calorimetry of PEPC.

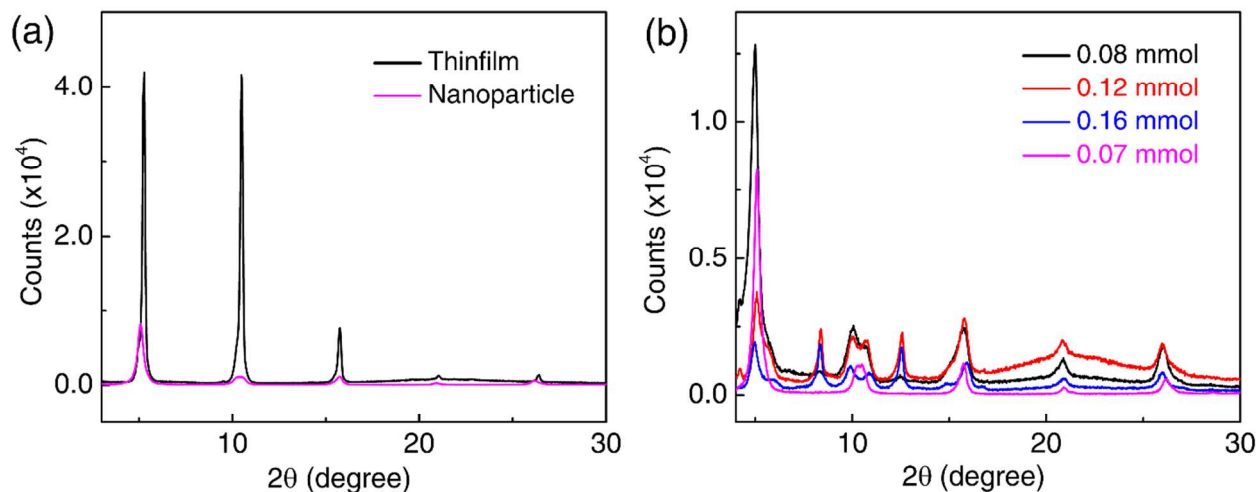


Figure S6. (a) XRD of thin film and nanoparticles of PEPC and (b) XRD patterns of drop casted thin films of nanoparticles produced with different amount of octylamine.

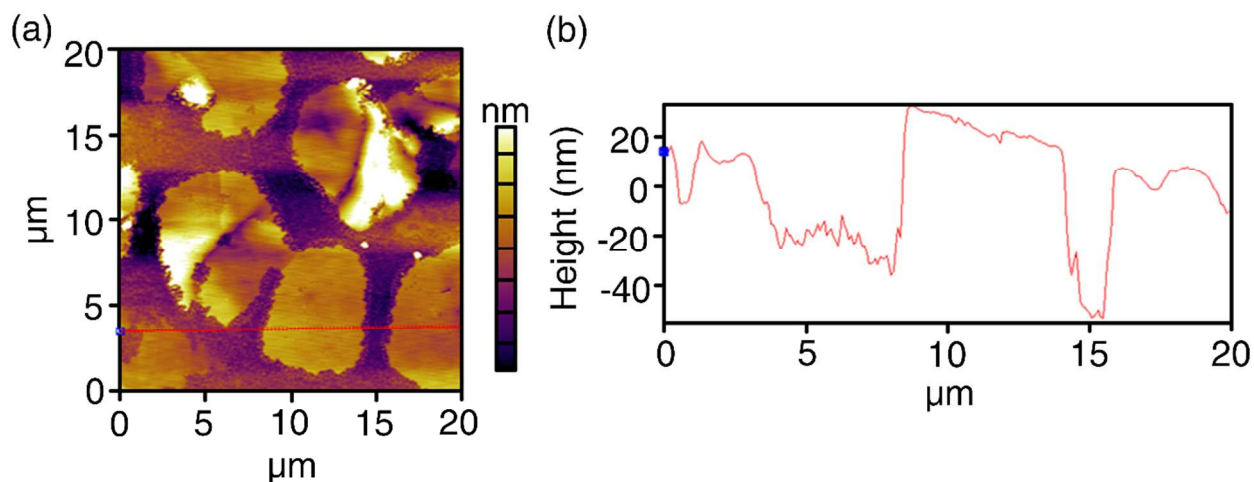


Figure S7. (a) Surface topography of a thin film produced using a 0.20 M solution of PEPC acquired by AFM and (b) height profile of the microdisks.

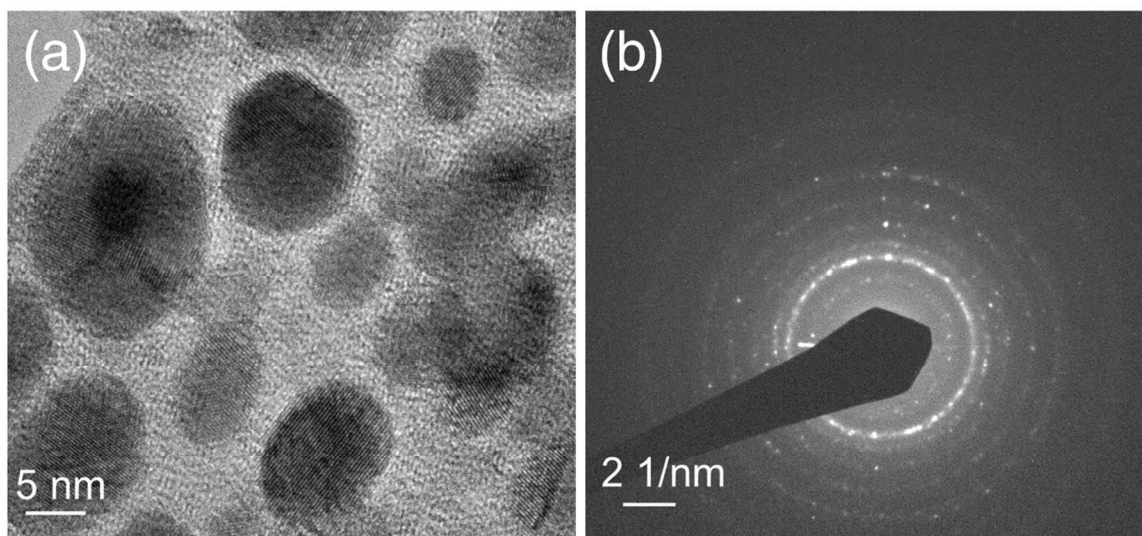


Figure S8. Electron microscopic images: (a) HRTEM. (b) SAED pattern.

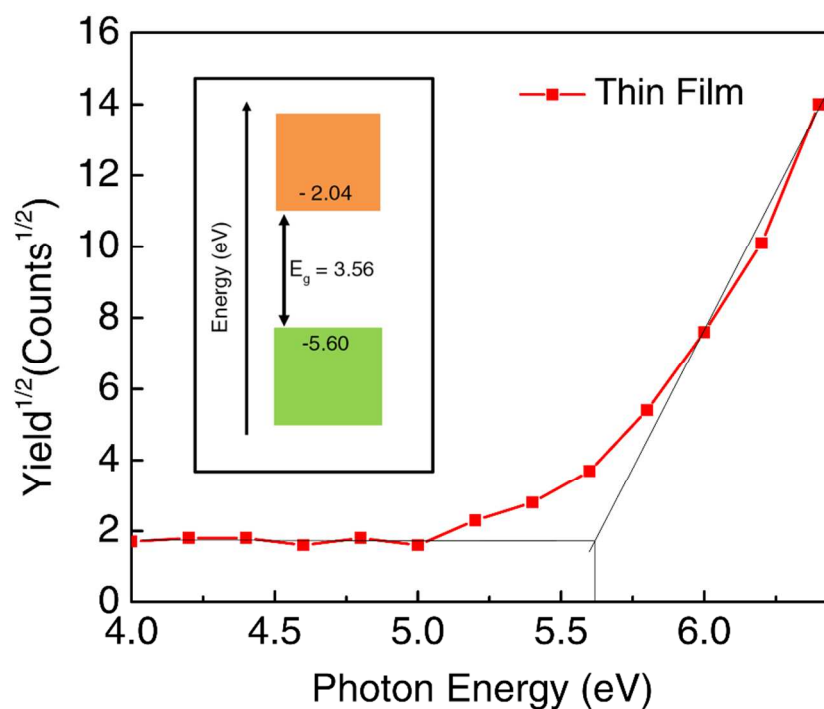


Figure S9. PESA analysis of a thin film of PEPC and the inset shows the energy level diagram of PEPC. The valence band maximum (VBM) of PEPC was estimated to be -5.6 eV using photoemission spectroscopy in air (PESA) (Figure S9) and the conduction band level was calculated as -2.04 eV using the optical band gap of material (3.56 eV). The VBM of this material is almost the same as the VBM of PEPB, which indicates that the halide variation does not influence the VBM.²¹

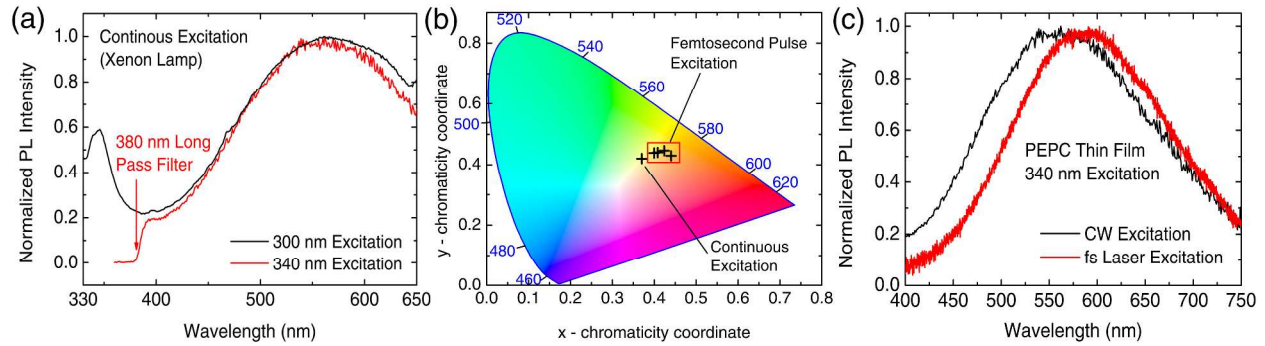


Figure S10. (a) PL Spectrum of PEPC thin film excited with 300 (with 320 nm long pass emission filter) and 340 nm (with 380 nm long pass emission filter) continuous wave source. The peak wavelength and FWHM is similar for these two excitation wavelengths. **(b)** CIE 1931 coordinates of the samples excited with either 340 nm continuous wave (for thin film sample) or 340 nm pulses (for powders, nanoparticles, single crystal and thin film samples) source. The CIE 1931 chromaticity diagram template was obtained from OriginLab Technical Support²². **(c)** Comparison of PL spectrum excited with 340 nm continuous wave and femtosecond excitation. A blue-shift in broad emission can be observed for the continuous wave excitation. The estimated blue-shift of around 75 meV is equivalent to a temperature difference of 870 K ($k_B T$) between the CW and fs excited cases. The small shift corresponds well with a Raman mode around 77 meV (Figure S16). A 380 nm long pass emission filter is used for the continuous wave excitation measurement. Response corrections have been performed for both spectra.

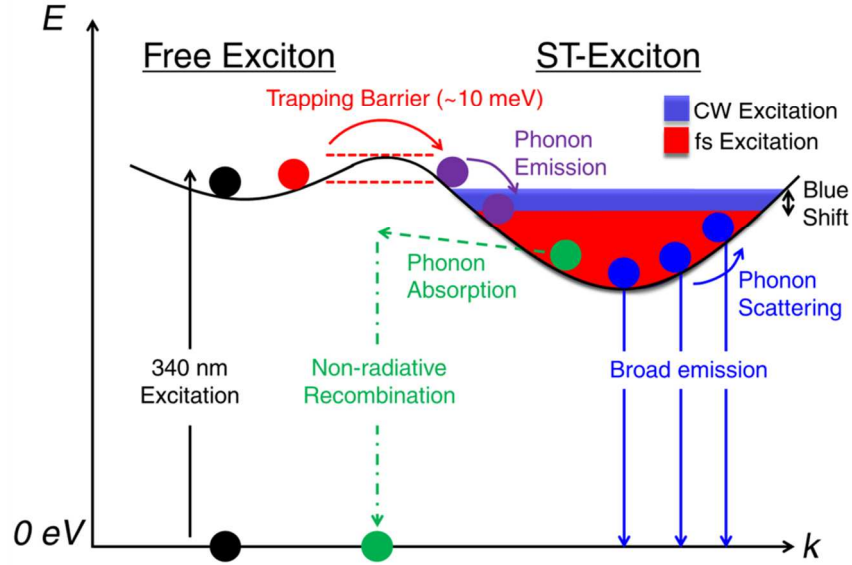


Figure S11. Schematic summarizing the main mechanism responsible for broadband emission in PEPC.

In the self-trapping process, the excitons scatter off the lattice that results in a shift and broadening of the exciton line. The presence of these excitons results in lattice deformation. The ensuing lattice stabilization gives rise to the self-trapping²⁴. As such, the presence of phonon is important for self-trapping, and could be generated via two methods: thermally generated phonon and exciton relaxation. The thermally generated phonon population (N_{phonon}) can be described by:

$$N_{phonon} = \left[\exp\left(\frac{\hbar\Omega_{phonon}}{k_B T}\right) - 1 \right]^{-1},$$

and is temperature dependent. It reduces at low temperature. On the other hand, phonon emission (Figure S15 - purple arrows), which is independent on phonon occupation number, still plays a role as scatter in the white emission. This means that phonon creation (emission) through phonon creation operator (a^\dagger):

$$a^\dagger |n\rangle = (n+1)^{1/2} |n+1\rangle$$

is temperature independent. Consequently, one still observes a broad band emission in Figure 4a - (phonon emission is still possible from relaxation of self-trapped excitons to the band minimum – Figure S15 - purple arrows) even at low temperatures.

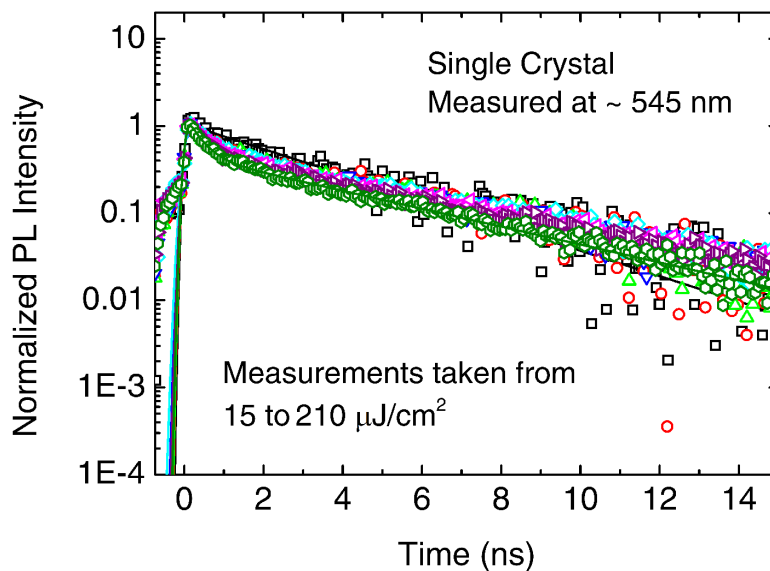


Figure S12. Normalized logarithmic plot of Figure 3a in the main manuscript.

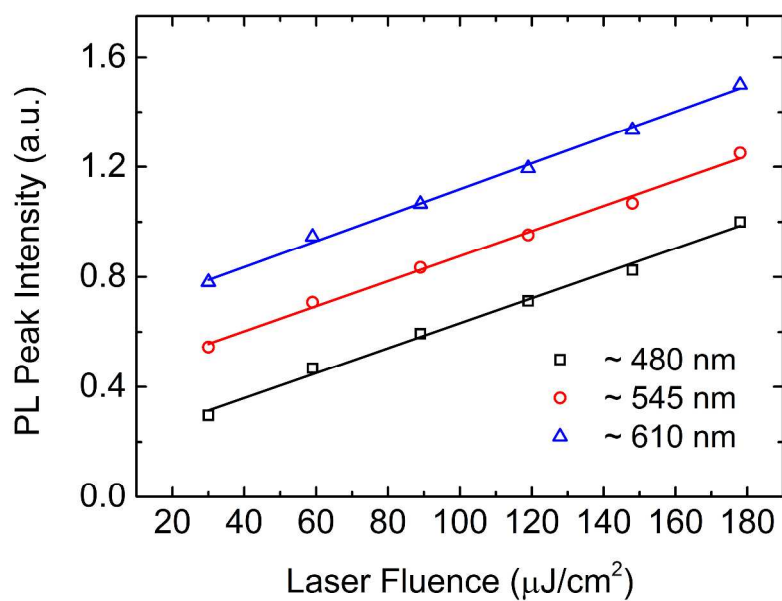


Figure S13. Steady-state PL peak intensities of PEPC single crystals as a function of laser fluence excited using 340 nm radiation. The peak intensity varies linearly with laser fluence with no saturation observed up to $\sim 180 \mu\text{J}/\text{cm}^2$.

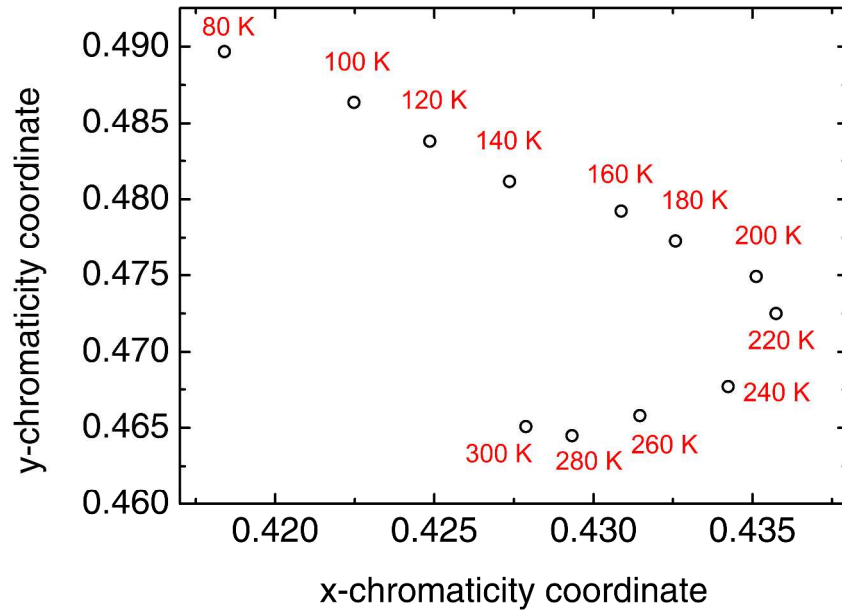


Figure S14. CIE 1931 coordinates of PEPC single crystals as a function of temperature from 80 K to 300K. No significant change in CIE coordinates with temperature was observed.

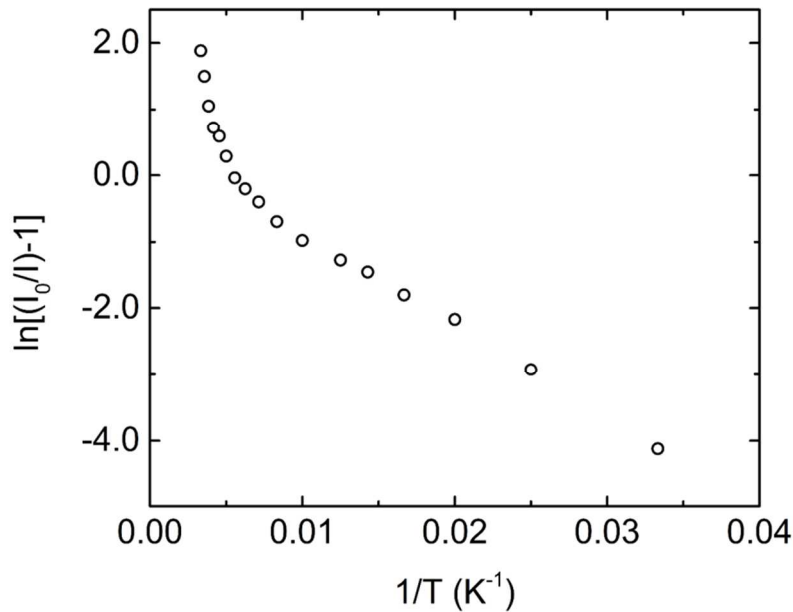


Figure S15. Plot of $\ln\left(\frac{I_0}{I}-1\right)$ against $\frac{1}{T}$ for Figure 4b. The symbols I , I_0 and T have the same meaning as those in equation (1) in the main text. A data set that obey mono-exponential Arrhenius fitting should show a linear relationship between $\ln\left(\frac{I_0}{I}-1\right)$ and $\frac{1}{T}$. The data shown in **Figure S13** clearly shows that a mono-exponential Arrhenius equation is insufficient to fit the experimental data and at least two exponentials are needed (shown in Figure 4b).

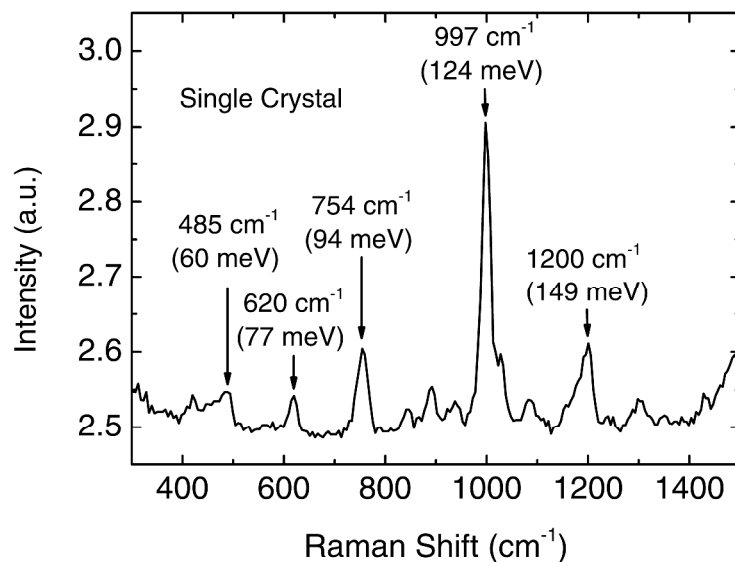


Figure S16. Room temperature Raman spectrum in the frequency range of 300 to 1500 cm^{-1} . The labeled Raman frequencies agree with the Raman modes of phenethylammonium chloride²³.

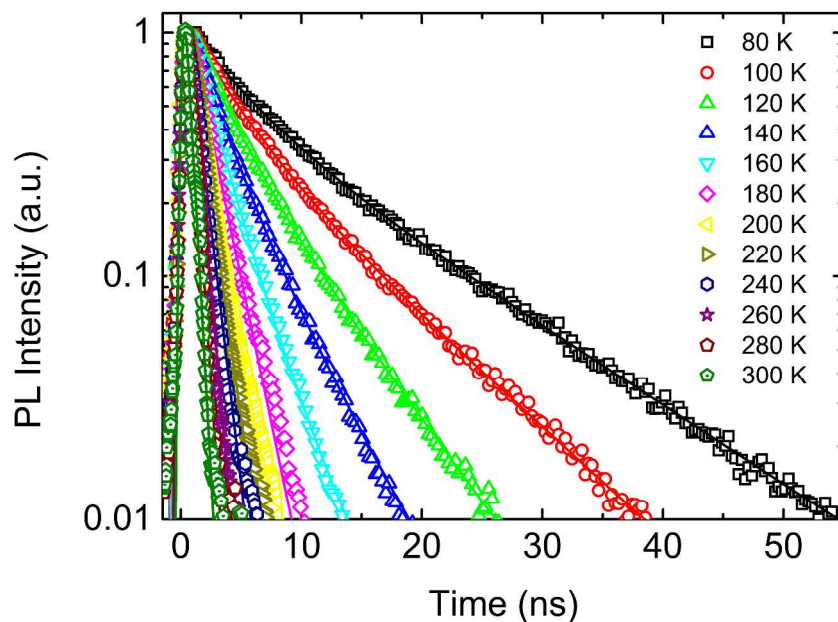


Figure S17. Temperature-dependent PL kinetics of PEPC single crystals showing significant PL lifetime lengthening at low temperatures. The experiment was conducted using 340 nm excitation with a laser fluence of $3.5 \mu\text{J}/\text{cm}^2$.

References

1. Sheldrick, G. M. C. N. U. o. G., Göttingen, Germany, 2008.
2. Sheldrick, G. M. T. U. o. G., Göttingen, Germany, 2008.
3. Hohenberg, P.; Kohn, W., Inhomogeneous Electron Gas. *Phys. Rev. B* **1964**, *136* (3B), 864-871.
4. Kohn, W.; Sham, L. J., Self-Consistent Equations Including Exchange and Correlation Effects. *Phys. Rev.* **1965**, *140* (4A), 1133-1138.
5. Kresse, G.; Hafner, J., Ab initio Molecular Dynamics for Liquid Metals. *Phys. Rev. B* **1993**, *47* (1), 558-561.
6. Kresse, G.; Furthmüller, J., Efficient iterative schemes for ab initio total-energy calculations using a plane-wave basis set. *Phys. Rev. B* **1996**, *54* (16), 11169-11186.
7. Perdew, J. P.; Burke, K.; Ernzerhof, M., Generalized gradient approximation made simple. *Phys. Rev. Lett.* **1996**, *77* (18), 3865-3868.
8. Blochl, P. E., Projector Augmented-Wave Method. *Phys. Rev. B* **1994**, *50* (24), 17953-17979.
9. Kresse, G.; Joubert, D., From ultrasoft pseudopotentials to the projector augmented-wave method. *Phys. Rev. B* **1999**, *59* (3), 1758-1775.
10. Monkhorst, H. J.; Pack, J. D., Special Points for Brillouin-Zone Integrations. *Phys. Rev. B* **1976**, *13* (12), 5188-5192.
11. Blochl, P. E.; Jepsen, O.; Andersen, O. K., Improved Tetrahedron Method for Brillouin-Zone Integrations. *Phys. Rev. B* **1994**, *49* (23), 16223-16233.
12. Davidson, E. R. In *Matrix Eigenvector Methods*, Methods in Computational Molecular Physics, Bad Windsheim, West Germany, August 1982; Diercksen, G. H. F.; Wilson, S., Eds. D. Reidel Publishing Company: Bad Windsheim, West Germany, 1982; pp 95-113.
13. Hestenes, M. R.; Stiefel, E., METHODS OF CONJUGATE GRADIENTS FOR SOLVING LINEAR SYSTEMS. *J. Res. Natl. Bur. Stand.* **1952**, *49* (6), 409-436.

14. Kleinman, L., Relativistic Norm-Conserving Pseudopotential. *Phys. Rev. B* **1980**, *21* (6), 2630-2631.
15. Macdonald, A. H.; Pickett, W. E.; Koelling, D. D., A Linearized Relativistic Augmented-Plane-Wave Method Utilizing Approximate Pure Spin Basis Functions. *J. Phys. C* **1980**, *13* (14), 2675-2683.
16. Tkatchenko, A.; Scheffler, M., Accurate Molecular Van Der Waals Interactions from Ground-State Electron Density and Free-Atom Reference Data. *Phys. Rev. Lett.* **2009**, *102* (7).
17. Bultinck, P.; Van Alsenoy, C.; Ayers, P. W.; Carbo-Dorca, R., Critical analysis and extension of the Hirshfeld atoms in molecules. *J Chem. Phys.* **2007**, *126* (14), 144111.
18. Setyawan, W.; Curtarolo, S., High-throughput electronic band structure calculations: Challenges and tools. *Comput. Mater. Sci.* **2010**, *49* (2), 299-312.
19. Aroyo, M. I.; Orobengoa, D.; de la Flor, G.; Tasci, E. S.; Perez-Mato, J. M.; Wondratschek, H., Brillouin-zone database on the Bilbao Crystallographic Server. *Acta Crystallogr A* **2014**, *70*, 126-137.
20. Momma, K.; Izumi, F., VESTA 3 for three-dimensional visualization of crystal, volumetric and morphology data. *J Appl. Crystallogr.* **2011**, *44*, 1272-1276.
21. Liang, D.; Peng, Y.; Fu, Y.; Shearer, M. J.; Zhang, J.; Zhai, J.; Zhang, Y.; Hamers, R. J.; Andrew, T. L.; Jin, S., Color-Pure Violet-Light-Emitting Diodes Based on Layered Lead Halide Perovskite Nanoplates. *ACS Nano* **2016**.
22. Support, O. T. Chromaticity Diagram Template.
<http://www.originlab.com/fileExchange/details.aspx?fid=168>.
23. Xie, M.; Qi, Y.; Hu, Y., Conformational Equilibrium and Hydrogen Bonding in Liquid 2-Phenylethylamine Explored by Raman Spectroscopy and Theoretical Calculations. *The Journal of Physical Chemistry A* **2011**, *115* (14), 3060-3067.
24. Toyozawa, Y., Dynamics and instabilities of an exciton in the phonon field and the correlated absorption-emission spectra. *Pure Appl. Chem* **1997**, *69* (6), 1171-1178.